JOURNAL OF SPACECRAFT AND ROCKETS
Vol. 46, No. 1, January–February 2009

Orbital Delivery of Small Payloads Using Hypersonic Airbreathing Propulsion

Michael K. Smart*
University of Queensland, Brisbane, Queensland 4072, Australia
and
Matthew R. Tetlow†
University of Adelaide, Adelaide, South Australia 5005, Australia

DOI: 10.2514/1.38784

Scramjet engines promise significantly higher specific impulse than rockets during the hypersonic phase of low-Earth-orbit insertion trajectories. Despite this, scramjets are not used on any current systems due to the difficulty of operating over the large Mach number envelope required by this accelerating trajectory. The key to taking advantage of airbreathing hypersonic engines for low-Earth-orbit insertion is to develop a multistage system that makes use of the scramjet only within its high-performance regime. A multistage rocket-scramjet-rocket system that accepts this limitation has therefore been examined. This system includes a solid rocket boost to Mach 6, a near-term Mach 6–12 hydrogen-fueled scramjet engine to propel a reusable second stage, and a liquid-fueled final-stage rocket. Trajectory calculations for a system scaled to deliver approximately 100 kg to a 200 km equatorial orbit indicate payload mass fractions of approximately 1.5% with the use of a scramjet stage designed for low drag and efficient packaging. The goal of this work is to guide the future development of scramjets by identifying the areas that will make the most significant improvement to their use for space access.

Nomenclature

A	=	area, m^2
C_D	=	drag coefficient
C_L	=	lift coefficient
D	=	drag, N
F	=	stream thrust, N
f	=	specific uninstalled thrust, m/s
f_{st}	=	stoichiometric ratio
g	=	gravitational acceleration, m/s^2
H_T	=	total enthalpy, J/kg
h	=	altitude, km
I_{sp}	=	specific impulse $[T/(w_f \times g)]$, s
$I_{sp_{net}}$	=	net specific impulse $[(T-D)/(w_f \times g)]$, s
L	=	lift, N
M	=	Mach number
m	=	mass, kg
m_c	=	mass capture ratio
p	=	pressure, Pa
q	=	dynamic pressure, Pa
T	=	temperature, K
T	=	thrust, N
u	=	velocity, m/s
w	=	mass flow rate, kg/s
w_{cap}	=	capture width of the scramjet, m
x	=	axial distance, m
α	=	angle of attack, deg
ζ	=	flight-path angle, deg
η	=	efficiency
ϕ	=	equivalence ratio

Subscripts

f	=	fuel
i	=	initial
m	=	mixing
n	=	nozzle
p	=	payload
s	=	structural
0–10	=	scramjet engine stations

I. Introduction

USE of airbreathing hypersonic propulsion for access to space has long been seen as a means of allowing aircraftlike operations to space. In fact, this was the basis for the National Aero Space Plane (NASP) Program conducted in the United States from 1986 to 1995 [1,2]. At that time, the creation of a single-stage vehicle that could operate from horizontal takeoff to low Earth orbit (LEO) and return to a horizontal landing was found to be well beyond the available technology. The same is true today, not because hypersonic airbreathing propulsion technology has not developed since the NASP program, but because the premise of a single-stage-to-orbit system is too restrictive. Results from the standard rocket equation for gravitationless drag-free flight,

$$\Delta u = g I_{sp} \ell_n \lfloor m_i/(m_p + m_s) \rfloor \tag{1}$$

plotted in Fig. 1, clearly show the significant improvement in payload mass fraction available from multistage systems. Although this analysis does not account for the lift available with airbreathing propulsion systems, the rocket equation tells current-day researchers the same thing it told the NASA engineers of the 1960s: getting to orbit is much easier with a staged vehicle.

Airbreathing propulsion does not change this basic premise. In fact, it reinforces it, because airbreathing propulsion systems only work over a portion of the velocity envelope required for accelerating to LEO. Figure 2 shows the estimated uninstalled specific impulse of different types of airbreathing propulsion systems from Mach 0–15 using hydrogen fuel. Up to Mach 4, turbojets are the most efficient. Above this speed, material issues related to the turbomachinery make turbojets difficult to operate, and ramjets are the most efficient. Above Mach 6, the supersonic combustion ramjet (scramjet) takes

Presented as Paper 8019 at the Hypersonic and Spaceplanes Conference, Canberra, Australia, 1–6 October 2006; received 28 May 2008; revision received 20 August 2008; accepted for publication 20 August 2008.

*Professor, Centre for Hypersonics. Senior Member AIAA.
†Research Fellow, School of Mechanical Engineering. Member AIAA.

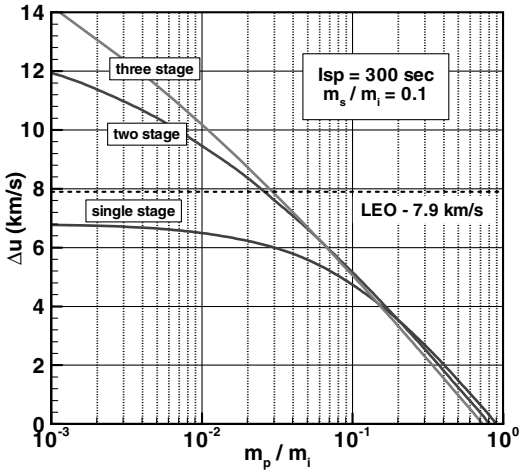

Fig. 1 Payload mass fractions calculated using the rocket equation, assuming that the total Δu is divided equally between the stages.

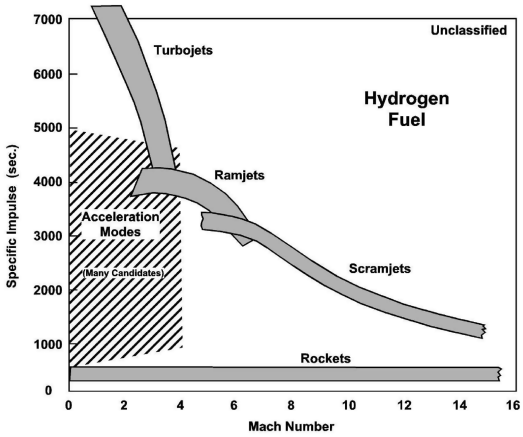

Fig. 2 Uninstalled specific impulse levels of different propulsion systems (NASA).

over as the most efficient system, as losses associated with slowing the air to subsonic speed are avoided. For comparison, Fig. 2 also shows the relatively low efficiency of rockets. This is due to the fact that rocket systems must store and pump both fuel and oxidizer. A significant number of systems studies for multistage access to space using some combination of rocket and airbreathing propulsion have been completed since the early 1990s, indicating that airbreathing stages can improve performance and add flexibility if used in the right way [3,4].

The current research accepts both preceding limitations:

1) A multistaged vehicle is needed for near-term access to space.

2) Any airbreathing propulsion engine used for space access can only operate for a portion of the flight.

Turbojets are a possible candidate for the initial phase of a flight to LEO, but they are currently limited to Mach 3+. Scramjets are a desirable candidate for the middle phase, particularly if the upper limit of their operation can be stretched to Mach 10+. However, scramjet use in conjunction with turbojets is problematic, as the takeover Mach number of a scramjet designed to operate at Mach 10 and above is likely to be Mach 5–6 in the absence of radical variable geometry. Finally, an efficient liquid-fueled rocket is a desirable candidate for the last phase to LEO.

The particular system examined here is a rocket-scramjet-rocket three-stage vehicle. The first stage is a solid rocket, chosen for its simplicity of operation, despite its low efficiency. The second stage is a reusable scramjet-powered hypersonic vehicle that can operate between Mach 6 and 12. This is followed by a liquid-hydrogen-fueled rocket third stage to boost the payload to LEO. The goal of this work is to investigate the performance advantages that a relatively near-term scramjet engine can bring to this multistage access-to-space system. A related goal is to use the results of this study to determine where future research into scramjets should be concentrated to have the greatest effect on the capabilities of this type of system. To accomplish these goals, considerable effort has been expended to develop a scramjet propulsion model that accounts for many real world constraints, including 1) variation of mass capture and specific thrust with vehicle angle of attack and flight Mach number, 2) the need for both scramjet and dual-mode engine operation, and 3) underexpanded nozzles. The performance of solid rocket boosters and liquid-hydrogen upper-stage rockets are well understood, and are simply modeled here with a schedule of specific impulse versus altitude for the first-stage booster, and a constant specific impulse for the orbital-stage rocket.

The paper includes a brief survey of existing rocket-based launch systems, followed by a description of the current system of interest, which is designed to boost an approximately 100 kg payload to a 200 km orbit. Next is a short description of the methods and assumptions used to calculate the trajectory of each stage, followed by a detailed description of the airbreathing propulsion model used for the scramjet-powered second stage. A baseline trajectory for the second stage is then discussed, and a payload mass fraction for the complete system is calculated. The paper closes with a summary and some conclusions.

II. Survey of Existing Launch Systems

To assess the performance of a new launch system, a comparison needs to be made with existing rocket-based launchers. As launch systems vary considerably in start mass and payload delivery capability, the payload mass fraction m_p/m_i is the best comparative measure of performance. Table 1 shows payload mass fractions for current small payload launch vehicles to low Earth orbit [5]. As expected, higher-altitude orbits result in lower payload mass fractions, as do higher inclinations. A 200 km circular orbit is used for the present study and a payload mass fraction of 0.9% (corresponding to the Long March CZ1D vehicle) is a reasonable benchmark for comparison. Also included in Table 1 is the payload mass fraction for the Delta 2 launch vehicle [5], indicating the improved performance made possible by increased scale.

III. Three-Stage System for Launch to LEO

The proposed launch system consists of a solid-fuel rocket booster, a reusable hydrogen-fueled scramjet vehicle with an initial mass of 3000 kg, and a 1000 kg liquid-fueled rocket final stage that is housed in the payload bay of the scramjet-powered vehicle. It is envisaged that the second stage would undergo a controlled return and horizontal landing after final-stage deployment. Some details of each stage are as follows:

Table 1 Current launch-vehicle performance

Launch vehicle	Payload mass (fraction)	LEO altitude and inclination
Augmented Satellite Launching Vehicle (India)	150 kg (0.36%)	400 km at 43 deg
M-3S11 (Japan)	780 kg (1.26%)	185 km at 31 deg
Long March CZ1D (China)	720 kg (0.9%)	200 km at 28 deg
Start-1 (Russia)	360 kg (0.6%)	400 km at 90 deg
Delta 2 (United States)	5089 kg (2.21%)	185 km at 28 deg

A. Booster

The initial booster is required to accelerate the second stage from a ground launch to flight conditions suitable for operation of the scramjet. The requirements for the booster were that it place the 3000 kg second stage at an altitude of 27 km, traveling at Mach 6 with a flight-path angle of $\zeta = 0.0$ deg. To satisfy the low-flight-path-angle requirement, a two-stage booster with a coast between the first and second stages was used. A preliminary sizing of this booster was made using a 3-degree-of-freedom trajectory analysis assuming solid-fuel rocket motors with an I_{sp} of 270 s at sea level and 276 s in vacuum, a structural mass fraction of $m_s/m_i = 0.18$, and aerodynamic data from the Ariane 3 launch vehicle. Although these I_{sp} values are somewhat typical of solid rocket motors, a conservative value for structural mass fraction was used to account for aspects of a real system not included in this preliminary analysis. An initial mass of $m_i = 10,300$ kg was estimated using this method. Optimization of the boost trajectory or use of a higher-performing rocket would lead to a reduced m_i. Furthermore, an alternative restartable single-stage booster may be a good tradeoff between performance and system complexity. Neither of these performance enhancements was considered in the current study.

B. Scramjet-Powered Hypersonic Vehicle

During the NASP program, a significant amount of work was performed on the types of vehicles that can fly hypersonically but still operate at low speed and land on a conventional runway. One vehicle examined during this period was the conical accelerator shown in Fig. 3. This winged-cone vehicle (WCV) [6] has a conical forebody (5 deg half-angle), a fuselage-centerline-mounted wing, a cylindrical section for engine installation, and a cone–frustrum aftbody with a vertical tail. The canards shown in Fig. 3 were only to be deployed at subsonic speeds. This vehicle was planned to be 200 ft in length, and its aerodynamic characteristics were verified by subscale wind-tunnel testing from low-subsonic to hypersonic Mach number [7].

A scaled-down version of this WCV was used as a candidate vehicle for the second stage of the current access-to-space system. From the predetermined start mass of 3000 kg and the average density for a hydrogen-fueled hypersonic vehicle of 124 kg/m^3 (taken from [8]), the volume of the vehicle is 24.19 m^3. Reducing the scale of the WCV vehicle to match this volume results in a vehicle with a length of 16.66 m, a cylinder diameter of 2.10 m, and reference area $A_{planform} = 24.01$ m^2. The aerodynamic force and moment characteristics of this vehicle were calculated using the aerodynamic preliminary analysis system in [6] for flight Mach numbers between 0.3 and 20. Based on the calculated data tabulated in [6], the following formulas for the variation of C_L and C_D with vehicle angle of attack α and flight Mach number have been developed for $M_0 > 5$ [9]:

$$C_L = C_{L\alpha} \times \alpha \tag{2}$$

$$C_D = C_{D0} + C_{D\alpha} \times \alpha^2 \tag{3}$$

with

$$C_{L\alpha} = 1.3 \exp\left[-\frac{(M_0 - 1)}{3}\right] + 0.6$$

$$C_{D0} = 0.04 \exp\left[-\frac{(M_0 - 1)}{3.2}\right] + 0.004$$

$$C_{D\alpha} = 1.3 \exp\left[-\frac{(M_0 - 1)}{2.5}\right] + 0.820702$$

Figures 4a–4c show the variations of C_L, C_D, and L/D for Mach numbers of 6, 8, 10, and 12, indicating that the maximum vehicle L/D occurs at $\alpha \sim 4$ deg. These coefficients are used in the current study for the scramjet-powered phase of the trajectory.

The scramjet propulsion system used in the study is based on the rectangular-to-elliptical shape-transition (REST) scramjet configuration [10,11]. This is a three-dimensional fixed-geometry scramjet flowpath that is integrated with the vehicle forebody, transitions from a rectangular capture area to an elliptical throat, and includes an elliptical combustor. The particular configuration used here was developed for flight between Mach 6 and 12 with hydrogen fuel and is referred to as the RESTM12 scramjet. Two views of how multiple RESTM12 modules would appear installed on the WCV are shown in Fig. 5. Three-degree-of-freedom trajectory simulations were performed for the second stage using this vehicle, assuming a fuel mass of 800 kg (fuel fraction of 0.267) and a structural mass of 1200 kg (structural fraction of 0.40). Assuming a fuel density of 71 kg/m^3 consistent with liquid hydrogen, 800 kg of fuel corresponds to 11.27 m^3, which is 46.6% of the entire vehicle volume.

C. Orbital Stage

The orbital stage was assumed to be a 1000 kg rocket plus a payload that would be deployed from the scramjet vehicle payload bay and accelerate from scramjet shutdown conditions to the required 200 km circular orbit. Typical upper-stage rockets use liquid

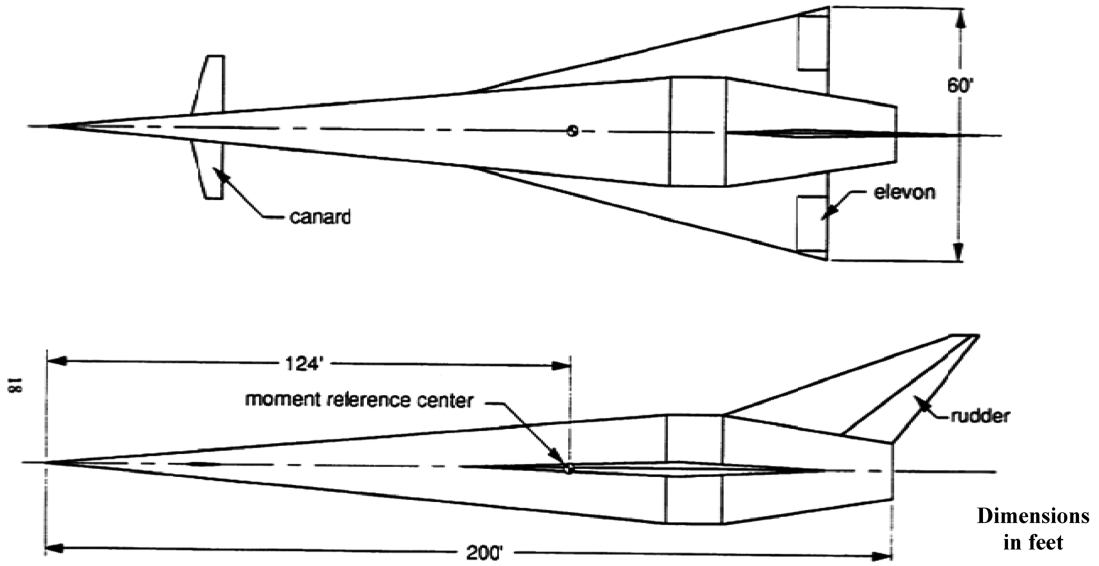

Fig. 3 WCV configuration ([6]).

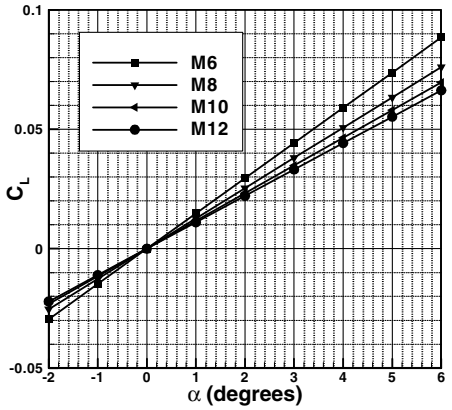

a) C_L vs angle of attack

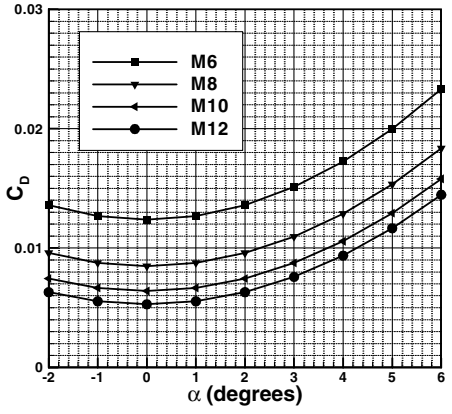

b) C_D vs angle of attack

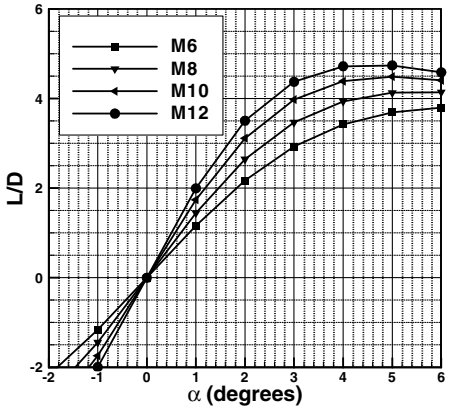

c) L/D vs angle of attack

Fig. 4 WCV aerodynamic coefficients.

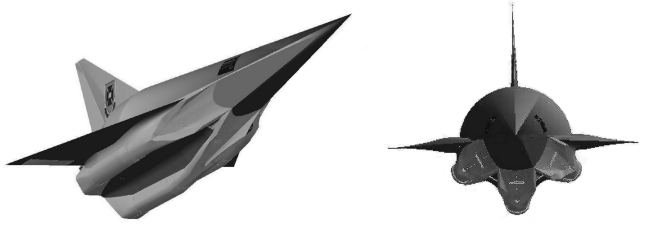

Fig. 5 Two views of the WCV with three RESTM12 scramjet propulsion modules installed.

oxygen and hydrogen as propellant and can produce I_{sp} levels greater than 400 s with structural mass fractions less than 0.1. The calculation of the upper-stage trajectory was accomplished here using a Hohmann transfer analysis and does not take into account the Δu losses associated with the staging of a real system. To account for this, conservative values of $I_{sp} = 324$ s and structural mass fraction of 0.15 were used for the upper stage in this study.

IV. Trajectory Simulation

The software used for trajectory simulation in this article was originally developed at the Space Systems Institute in Stuttgart, Germany. The dynamic equations were taken from [12] and describe a 3-degree-of-freedom trajectory over a rotating Earth model using a fourth-order Runge–Kutta integration technique. A spheroidal Earth model was used to determine the radius of the Earth at given latitudes. A fourth-order gravitational model [13] was implemented to approximate the Earth's gravitational field, and the atmospheric parameters were calculated using the Mass Spectrometer Incoherent Scatter Experiment 1993 atmosphere model [14].

Three-degree-of-freedom trajectory simulations were performed for the first-stage booster and the second-stage scramjet, with a Hohmann transfer analysis used for the orbital stage. The scramjet flight phase was controlled using a parameter set of angle of attack as a function of time. The aim of the control strategy was to accelerate from Mach 6 to as high a velocity as possible at a dynamic pressure close to 50 kPa, using a predetermined fuel mass of 800 kg. Numerous runs were performed to understand the dominant parameters governing the trajectory, however, no trajectory optimization was performed in this preliminary study.

V. Scramjet Propulsion Module

A realistic model for the thrust produced by an airframe-integrated scramjet must account for the effects of changing flight Mach number M_0, vehicle angle of attack α, and dynamic pressure q_0 on 1) inlet capability and operability limits, 2) fuel–air mixing characteristics, 3) fuel–air combustion physics, 4) engine operability limits, 5) internal flowpath drag and heat loss, and 6) nozzle expansion ratio.

The propulsion module used for the current research accounts for the effects of M_0, α, and q_0 on all these factors. It was developed from the calculated performance of a fixed-geometry REST scramjet engine that has a design point of $M_0 = 12.0$, but remains operational down to $M_0 = 6.0$. This engine will be referred to here as the RESTM12 scramjet and is considered to be a near-term engine that could be envisaged to fly within 5–10 years. Some preliminary ground testing of this engine has shown promising results [15].

During a trajectory calculation, the trajectory program makes calls to the propulsion module to obtain the specific thrust, specific impulse, and equivalence ratio of the engine for a particular flight velocity, angle of attack, and altitude. To supply this information, a propulsion database was created for the RESTM12 scramjet by analyzing 1) the vehicle forebody/inlet compression, 2) the combustion of fuel and air in the combustor, and 3) the expansion process in the nozzle. Figure 6 shows a schematic of the internal flowpath of an airframe-integrated scramjet with particular reference stations highlighted. In keeping with convention [16], station 0 is in the freestream flow ahead of the engine, and a stream tube with area A_0 is captured and processed by the engine. Station 1 is downstream of the vehicle forebody shock and represents the properties of the flow that enters the inlet. Station 2 is at the inlet throat, which is usually the minimum area of the flowpath. Station 3 is at the start of the combustor, and fuel and air is mixed and burned by the end of the combustor at station 4. The nozzle includes an internal expansion up to station 9 and an external expansion to station 10 at the end of the vehicle.

A. Engine Installation on the Vehicle

The RESTM12 scramjet is designed to operate at $q_0 \sim 50$ kPa in conjunction with a vehicle forebody compression equivalent to that

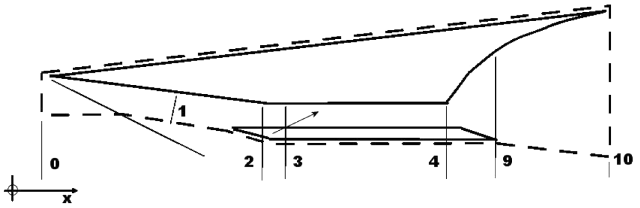

Fig. 6 Flow stations for engine analysis.

generated by a 6 deg wedge. Analysis of the WCV vehicle conical forebody over the Mach 6–12 flight regime indicated that it generated the desired precompression at $\alpha = 2$ deg. Given this, the nominal angle of attack for the vehicle was assumed to be $\alpha = 2$ deg. Hence, the engine was installed on the vehicle so that its combustor section was parallel with the velocity vector when the vehicle was at $\alpha = 2$ deg. The operational angle-of-attack range for the engine was assumed to be ± 3 deg. about the nominal, and so the angle-of-attack limits for the vehicle were set to $\alpha = -1$ and $+5$ deg. It was assumed that the vehicle could be trimmed such that the pitching moment was zero at all times. As shown in Fig. 4, the vehicle had minimum drag and essentially zero lift at $\alpha \sim 0$ deg. Three RESTM12 scramjet modules were used for the trajectory calculations, each with a width of $w_{\text{cap}} = 0.76$ m. This scale allowed smooth integration with the 16.66-m-long WCV vehicle (Fig. 5).

B. Compression Model

The forebody and inlet combine to produce the required compression for the engine. The forebody compression was modeled as being equivalent to a 6 deg two-dimensional shock when the vehicle is flying at its nominal orientation of $\alpha = 2$ deg. Angles of attack greater than or less than the nominal add to or subtract from the equivalent shock angle of the forebody, respectively. The inlet compression was determined using polynomial fits to capability parameters determined from a set of computational fluid dynamics (CFD) solutions of the RESTM12 inlet at $M_0 = 6.0$, 8.0, 10.0, and 12.0; $\alpha = 2$ deg; and $q_0 = 50$ kPa. These CFD solutions were calculated with the NASA Langley Research Center code VULCAN [17] on a 2-million-cell grid using wall functions to model boundary-layer phenomena. A thermally perfect model was used for the air, and flow was assumed to be turbulent from the forebody leading edge. Figure 7 shows the symmetry-plane Mach number contours for the inlet when the vehicle is flying at $M_0 = 10$, $q_0 = 50$ kPa, and $\alpha = 2$ deg, corresponding to $M_1 = 7.950$. Note that the highly notched cowl allows flow spillage when M_1 is below the design point for the inlet ($M_1 = 9.113$). The inlet was assumed to remain operational at overspeed conditions ($M_1 > 9.113$), but with its capability and mass capture limited to that calculated at $M_1 = 9.113$. In practice, oversped operation will lead to heating issues in the inlet and would not be desirable for long periods.

The RESTM12 inlet has a geometric contraction ratio of 6.61 and an internal contraction ratio of 2.26. Inlets of this class have been shown in experiments to self-start at internal contraction ratio values significantly higher than the Kantrowitz limit [18]. Based on these experiments, the lower limit for self-starting of the RESTM12 inlet was estimated to be $M_1 = 5.0$. Figure 8 shows the variation of some important inlet capability parameters with M_1. These polynomial fits

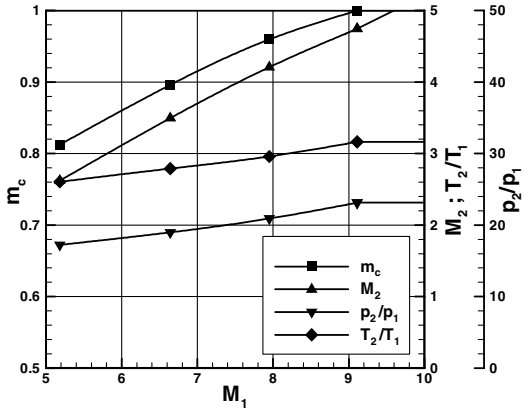

Fig. 8 RESTM12 inlet capability parameters.

to the CFD database were used in the thrust module to calculate the stream-thrust-conserved one-dimensional flow conditions and mass flow rate at the inlet throat (station 2).

C. Combustor Model

The processes of fuel addition, fuel–air mixing, and combustion are modeled in this study using a stream-thrust-based cycle analysis that conserves mass, momentum, and energy with the assumption of quasi-one-dimensional flow. Both pure supersonic combustion and dual-mode combustion (combined subsonic/supersonic) are modeled using the methodology described in [19]. At conditions in which the combustion-generated pressure rise is such that flow separation occurs, a diffuser model [20] is used to estimate the effects of the shock train that forms upstream of fuel injection. This model enables engine operability limits to be established, limiting the maximum fuel equivalence level for the engine in these instances. The combustor flows of interest are modeled as mixtures of thermally perfect gases that are in thermodynamic equilibrium. Furthermore, the combustion of fuel is assumed to be *mixing-limited*, meaning that once the fuel is allowed to mix with the air, the mixture immediately goes to an equilibrium state of fuel, air, and combustion products.

Figure 9 shows a schematic of a scramjet combustor with air entering from the left at station 2, fuel injection at station 3, and combustion products exiting to the right at station 4. The gross parameters for the air entering the combustor are mass flow rate w_2, stream thrust F_2, and total enthalpy H_{T2}. The incoming flow area is A_2. The gross parameters associated with fuel injection are fuel flow rate w_f, fuel stream thrust F_f, and fuel total enthalpy H_{Tf}. As the fuel–air mixture travels downstream, a proportion of the fuel is allowed to react with the air, and the gross parameters of the flow are calculated by conserving mass, momentum, and energy using a control volume analysis associated with incremental steps of length Δx along the combustor. Through calls to thermodynamic equilibrium routines, state properties and the velocity are determined at all stations along the combustor.

In a typical combustor calculation the area distribution of the combustor is specified a priori. The amount of fuel that is allowed to react with the air at a particular station is dictated by a mixing efficiency curve $\eta_m(x)$ that takes the form

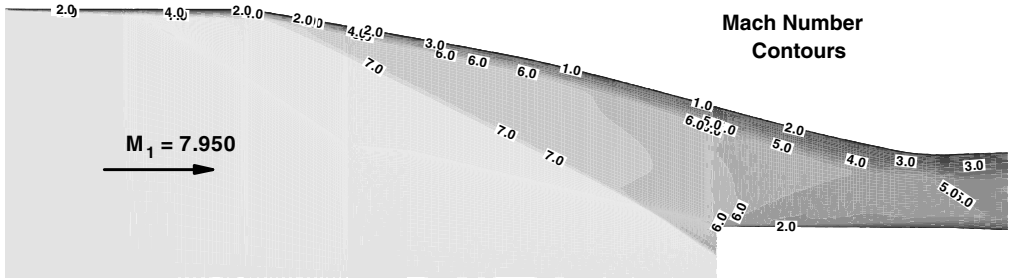

Fig. 7 Symmetry-plane Mach number contours in the RESTM12 inlet at $M_0 = 10$.

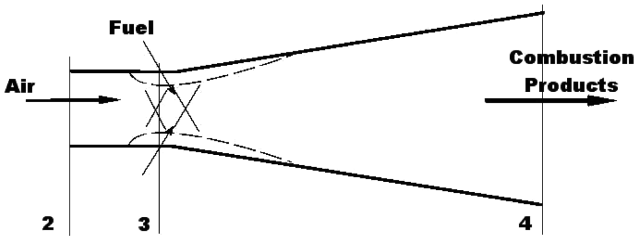

Fig. 9 Schematic of the combustor analysis.

$$\eta_m = \eta_{m,\text{tot}}\left[\frac{\vartheta X}{1+(\vartheta-1)X}\right] \tag{4}$$

where $\eta_{m,\text{tot}}$ is the mixing at the end of the combustor, $X = (x-x3)/(x4-x3)$, and ϑ is an empirical constant of order 1 to 10 that depends on the rate of mixing [16]. For the current study, $\eta_{m,\text{tot}}$ was set to 0.8 at all times and a value of $\vartheta = 2.0$ was used. These values correspond to robust operation of the engine and are consistent with preliminary experimental data [15]. The proportion of the fuel that has not mixed with the air is considered to be inert and is included as an unreacted species in the thermodynamic equilibrium calls. The incremental area change ΔA across a control volume of length Δx is known from the area distribution, and incremental changes to the stream thrust and total enthalpy from fuel combustion, friction forces, pressure forces, and heat loss are calculated to determine the stream thrust and total enthalpy of the flow exiting the control volume. The analysis starts at station 2 and marches along the combustor until station 4 is reached. Some iteration is required for cases in which dual-mode combustion occurs [19].

D. Nozzle Expansion Model

The RESTM12 engine nozzle includes both an internal expansion up to station 9 and an external expansion to station 10 at the end of the vehicle. In this study, the nozzle expansion was assumed to be defined by a fixed exit area ratio A_{10}/A_4 for all flight conditions. This method for determining the extent of the nozzle expansion is consistent with a fixed-geometry engine, but it is a simplification of the characteristics of a real scramjet engine plume expansion. In this model, A_{10} was set to be 80% of the A_0 at $M_0 = 12$ and $\alpha = 2$ deg, leading to significant underexpansion ($p_{10} > p_0$) for all flight conditions. Use of this value for A_{10} was expected to lead to a conservative level of uninstalled thrust for the engine. Higher fidelity can be added to this section of the propulsion module as the results of further experiments and analysis become available.

Typical losses in a scramjet nozzle are due to nonequilibrium chemistry (nozzle freezing), flow angularity, and viscous effects. These were modeled here by the use of a nozzle efficiency η_n, which was applied as a gross thrust coefficient as follows:

1) Given the conditions at station 4, expand the flow isentropically assuming chemical equilibrium from A_4 to A_{10} to obtain $F_{10,\text{isentropic}}$.

2) Apply the nozzle efficiency to the ideal stream thrust increment between stations 4 and 10 (i.e., $F_{10} = F_4 + \eta_n\,[F_{10,\text{isentropic}} - F_4]$)

Assuming no heat loss in the nozzle, calculate the remaining flow properties at station 10, consistent with F_{10}. A value of $\eta_n = 0.9$ was used in the study.

E. Propulsion Database

A database was created for the RESTM12 flowpath using the preceding compression, combustor, and nozzle expansion models. This was based on calculations performed for $M_0 = 6.0$, 8.0, 10.0, 12.0, and 14.0 at vehicle $\alpha = -2.0$, 0.0, 2.0, 4.0, and +6.0 deg and $q_0 = 50$ kPa. All calculations were performed with $\phi = 1.0$, except for the $M_0 = 6.0$ calculations, where the engine reached its operability limit at $\phi < 1.0$. This characteristic was due to the fact that the RESTM12 scramjet was designed with a contraction ratio and combustor divergence suitable for operation at $M_0 > 10$ and is one of the real-world compromises that must be made in a fixed-geometry engine. All calculations at $M_0 = 6.0$ involved dual-mode operation of the engine.

The three propulsion parameters required by the trajectory code were the uninstalled specific thrust $f = \Delta F/w_0 = (F_{10}-F_0)/w_0$, specific impulse of the engine $I_{\text{sp}} = \Delta F/(g \times w_f)$, and equivalence ratio $\phi = w_f/(f_{\text{st}} \times w_0)$. The calculations used in the database were performed for a single engine with a capture width $w_{\text{cap}} = 150$ mm (i.e., at wind-tunnel model scale). It was assumed that the propulsion parameters calculated in this way can be conservatively used for larger engines. Figure 10 shows contour plots of f and I_{sp} calculated for the RESTM12 engine in the current study, as well as the ϕ used. Note that even though the design point of the engine is Mach 12, f and I_{sp} are greatest at Mach 6. This gives a clear indication of the diminishing returns of scramjets as the Mach number increases.

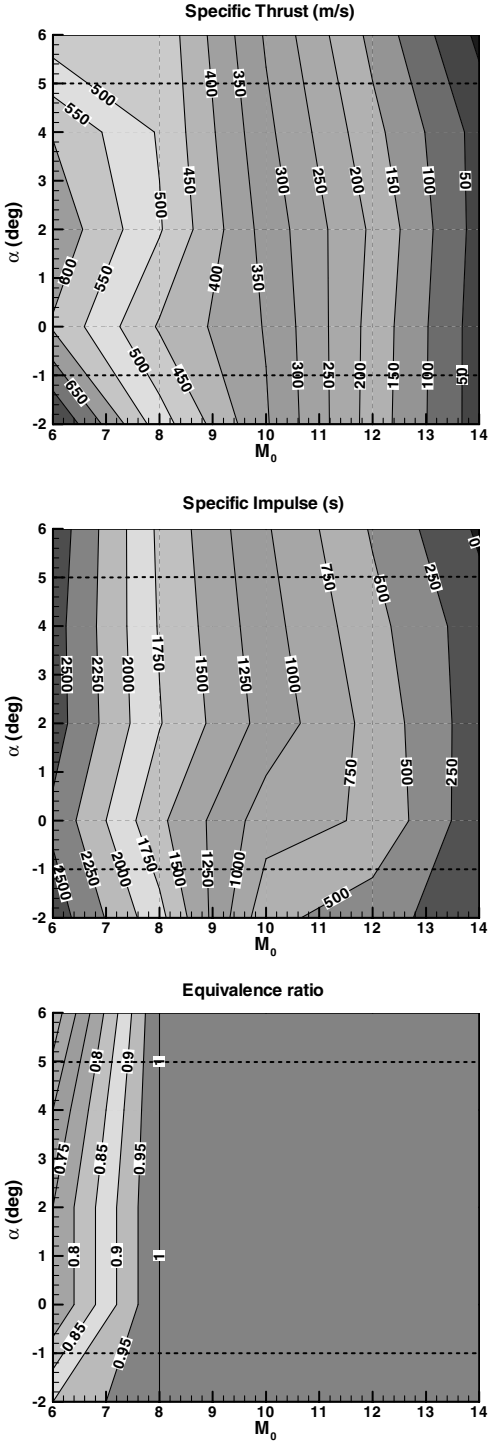

Fig. 10 RESTM12 scramjet performance database.

F. Force Accounting

The propulsion module accounts for flow changes between stations 0 and 10 (Fig. 6), and stream thrust changes between these stations represent the uninstalled internal thrust of the engine. We therefore have available for use in trajectory simulations the uninstalled thrust of the propulsion system and the aerodynamic coefficients for the vehicle without engine installation [Eqs. (2) and (3)]. Some simplifying assumptions have been made with regard to the force accounting to combine these two for the trajectory calculations of the integrated vehicle, as follows::

1) The propulsion system only generates net forces along the vehicle axis (i.e., thrust or drag). This means that any lift forces due to the installation of the engine (or its operation) are considered to not substantially contribute to the lift of the integrated vehicle. Therefore, all lift forces for the vehicle are based on Eq. (2).

2) The external drag of the propulsion system can be traded against the drag of the portion of the forebody that compresses the air entering the propulsion system. The drag from the portion of the vehicle forebody that compresses the air entering the propulsion system is included in both the propulsion database and the aerodynamic drag coefficient of the vehicle. To compensate for the double-accounting of this drag, the external drag of the propulsion system is assumed to be included in the aerodynamic drag coefficient of the vehicle [Eq. (3)]. This is a conservative assumption, as long as the external drag of the propulsion system is small. A front view of the vehicle with 3 RESTM12 propulsion systems installed is shown in Fig. 5. Because of the highly swept nature of the RESTM12 engines, the external surfaces of the propulsion system represent a very small proportion of the total frontal area of the integrated vehicle, which is consistent with this assumption.

3) The vehicle is trimmed at all angles of attack.

These assumptions are considered to b reasonable, given the exploratory nature of the current article. A more detailed determination of the aerodynamic characteristics of the integrated vehicle will be made for future studies of this kind.

VI. Baseline Scramjet-Powered Second-Stage Trajectory

The solid rocket booster delivered the 3000 kg scramjet-powered vehicle at an altitude $h = 27$ km, velocity $u_0 = 1804.5$ m/s, and flight-path angle $\zeta = 0.0$ deg. This corresponds to a flight Mach number $M_0 = 6.01$ and dynamic pressure $q_0 = 48.0$ kPa. The second-stage airbreathing trajectory was generated by setting a time schedule for vehicle angle of attack such that the vehicle remained at a dynamic pressure of approximately 50 kPa and was fueled at $\phi = 1.0$ or the maximum ϕ for stable engine operation. The second stage was shut down when the 800 kg of hydrogen fuel had been depleted, leaving a vehicle mass of $m = 2200$ kg.

Figure 11 shows plots of altitude and velocity versus time since staging for a baseline 456 s flight that covered 1372 km. The scramjet propulsion system was started immediately upon separation from the first stage. Setting the vehicle to an initial angle of attack of $\alpha = 1.8$ deg (close to the nominal angle of attack of 2 deg) generated thrust levels of $T = 41.03$ kN, drag of $D = 16.35$ kN, and lift of $L = 33.39$ kN ($L/D = 2.04$), leading to immediate acceleration and increase in altitude. As the trajectory progressed, the velocity and altitude continued to increase, with final values of $u_0 = 3704$ m/s and $h = 36.09$ km. Figure 12 shows plots of Mach number and dynamic pressure during the flight, along with the angle-of-attack schedule used. After a peak of $q_0 = 56.4$ kPa at $t = 22$ s after separation, the dynamic pressure was kept between 50 and 55 kPa for the remainder of the flight. The flight Mach number increased steadily to $M_0 = 8.0$ after $t \sim 100$ s, to $M_0 = 10.0$ after $t \sim 220$ s, and to a final value of $M_0 = 11.55$ at the completion of the second stage, which is just below the engine design point. Note that the α schedule to generate this trajectory ranged between $\alpha = 1.3$ and 1.8 deg (i.e., slightly below the nominal vehicle angle of attack and well below the maximum L/D for the WCV of $\alpha \sim 4$ deg).

Figure 13 shows plots of the thrust, drag, and lift for the vehicle throughout the second-stage trajectory, along with the L/D. Below

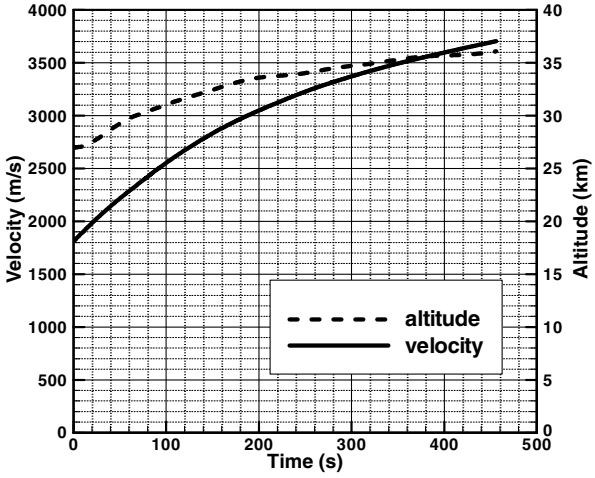

Fig. 11 Altitude and velocity of the baseline trajectory.

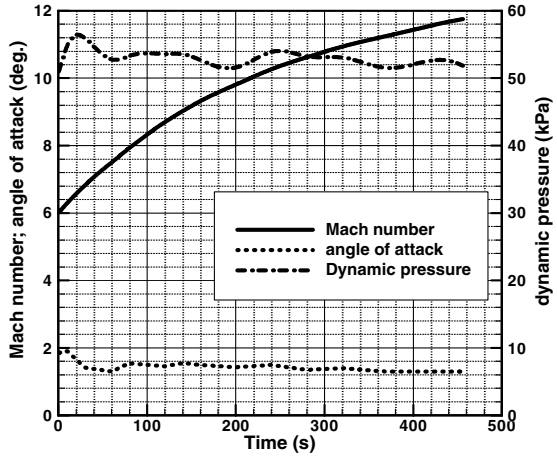

Fig. 12 Flight Mach number, angle of attack, and dynamic pressure of the baseline trajectory.

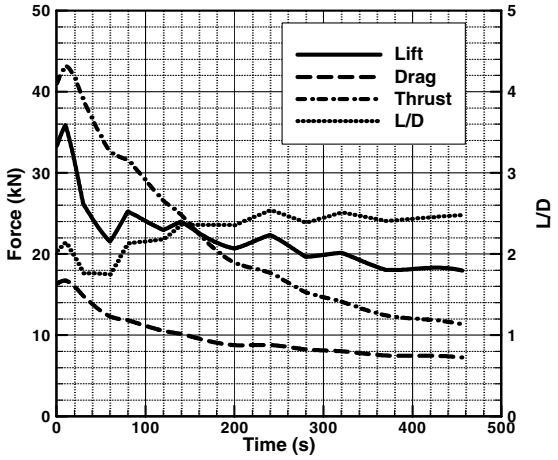

Fig. 13 Thrust, drag, lift, and L/D of the baseline trajectory.

Mach 8, the combination of the RESTM12 propulsion system and the WCV vehicle performed strongly with a thrust-to-drag ratio at Mach 8 of $T/D = 2.66$ and with $L/D = 2.14$. As the vehicle increased its Mach number, the T/D reduced due to the decreased specific thrust of the engine, indicating the inherent difficulty of using airbreathing propulsion at high hypersonic Mach numbers. However, due to the centrifugal effect, the L/D of the vehicle increased along the trajectory above its aerodynamic value, enabling

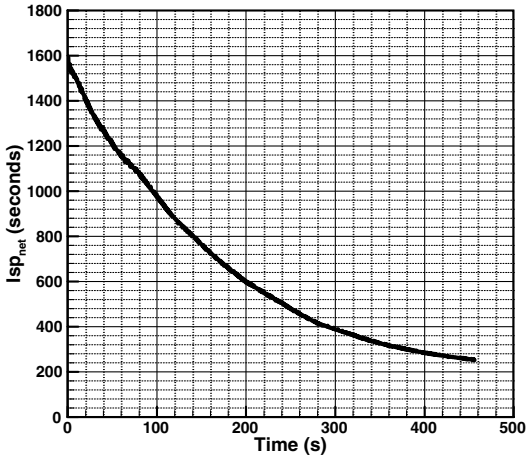

Fig. 14 Net I_{sp} along the baseline trajectory.

the vehicle to be flown at reduced α (and therefore reduced drag). Finally, Fig. 14 shows plots of $I_{sp_{net}} = (T - D)/(g \times w_f)$ during the flight. This is the key parameter that must be considered when comparing an airbreathing propulsion system with more traditional rockets. At the start of the second stage, the $I_{sp_{net}} \sim 1600$ s, a value significantly higher than a rocket. As speed increased, the $I_{sp_{net}}$ reduced, dropping to approximately 500 s at $t = 240$ s when the vehicle is flying at approximately Mach 10. The point in the trajectory when $I_{sp_{net}}$ drops below that of a rocket (typical 250–350 s) is a good indication of when the final staging should be performed. For the current system $I_{sp_{net}}$ drops to 300 s at $t = 382.5$ s when the flight velocity and altitude are 3561 m/s and 35.61 km, respectively.

Improvement in the scramjet phase would result from 1) increasing the $I_{sp_{net}}$ at Mach 10+, 2) matching the lift and weight of the vehicle such that it operated closer to its maximum L/D (in this case $\alpha \sim 4$ deg), and 3) optimization of the trajectory. In terms of the scramjet performance, the current study suggests that future research should be concentrated on improved thrust generation at Mach 10+. With regard to item 2, the fact that the vehicle flew at $q \sim 50$ kPa with $\alpha < 2$ deg suggests that the WCV generated more than enough lift, and that reduced wing area (i.e., reduced drag) would allow it to fly closer to its maximum L/D. With regard to item 3, the baseline scramjet-powered trajectory presented in this article was constrained to be close to $q \sim 50$ kPa. Optimization of the trajectory for maximum altitude and velocity for a given fuel mass within the operational α and q limits of the engine could lead to a better third-stage separation condition.

VII. Boost to LEO

The engine shutdown conditions at the end of the scramjet burn are an altitude of 36.09 km, a velocity relative to the local horizontal frame of 3704 m/s, and a flight-path angle of 0.309 deg. Assuming an easterly equatorial launch, this corresponds to an inertial velocity of 4169 m/s. The mass at scramjet shutdown is 2200 kg. Assuming that the structural mass of the WCV is 1200 kg, the upper-stage mass (payload and rocket) is 1000 kg. From the velocity, altitude, and flight-path angle at scramjet shutdown, the payload mass for a 200 km orbit was approximated using Hohmann transfers. This involved a transfer to achieve an orbit of 36.09×200 km and then another to achieve a circular 200 km orbit. Using orbital mechanics analysis, the required Δu to achieve a 200 km circular orbit from the scramjet shutdown conditions was 3811.8 m/s. Assuming a specific impulse of 324 s and a structural mass fraction of 0.15 for the upper stage, the payload delivered to orbit is estimated to be 151 kg. This corresponds to a payload fraction for the whole system of $m_p/m_i = 1.47\%$, which compares favorably with the value of 0.9% established as a benchmark for rocket-based systems of similar scale. This preliminary result is considered promising enough to justify future refinements to the analysis, including more detailed determination of the aerodynamic characteristics of the integrated second-stage vehicle and more detailed analysis of the Δu losses at the final staging so that less conservative I_{sp} and structural mass fraction values can be used for the orbital stage.

VIII. Conclusions

A low-Earth-orbit insertion trajectory was calculated for a rocket-scramjet-rocket system. The trajectory was based around a 3000 kg scramjet-powered vehicle that was designed to operate from Mach 6 to 12 using hydrogen fuel. A solid rocket booster was used to lift the vehicle to scramjet ignition conditions, and a liquid-hydrogen-fueled upper stage completed the boost to a 200 km circular orbit. The scramjet-powered second-stage vehicle was a winged-cone configuration for which an extensive series of hypersonic aerodynamic data was available. The scramjet propulsion system was a promising 3-D configuration that was designed to operate between Mach 6 and 12 with fixed geometry. The propulsion database developed for this engine accounted for many of the engineering constraints of a fixed-geometry scramjet, such as variation of mass capture, operability, and specific thrust with angle of attack and flight Mach number. A key assumption in the analysis is an average density of 128 kg/m^3 for a hydrogen-fueled hypersonic vehicle. Furthermore, conservative specific impulse and structural mass fraction values were used for the orbital-stage rocket to obtain realistically achievable payload mass fractions for the system as a whole.

The scramjet-powered vehicle was boosted to Mach 6.0 and an altitude of 27 km by the solid rocket booster. During the scramjet-powered phase of the trajectory, the angle of attack of the vehicle was adjusted to maintain a dynamic pressure of approximately 50 kPa. This was achieved with an angle-of-attack schedule that was well below the angle of attack for maximum lift/drag of the vehicle. Net positive thrust (engine thrust minus vehicle drag) was able to be maintained throughout the acceleration from Mach 6 to approximately Mach 11.55, and the scramjet was shut down after 456 s, once it consumed 800 kg of hydrogen fuel. The airbreathing second stage covered a distance of 1372 km and raised the vehicle altitude to 36.09 km and raised its velocity in the local horizontal frame to 3704 m/s.

The third-stage rocket boosted the payload to a 200 km circular orbit using Hohmann transfers. Assuming an easterly equatorial launch, a payload of 151 kg could be delivered to orbit. This corresponds to a low-Earth-orbit payload mass fraction of 1.47%, which compares favorably with existing rocket-based systems for small payloads of approximately 0.9%. This promising result for a rocket-scramjet-rocket system could be improved through 1) higher net I_{sp} at Mach 10+ scramjet operation, 2) second-stage trajectory optimization, and 3) a more efficient first-stage booster. Future analyses of this type of system should also include refinements to the calculation of the aerodynamic characteristics of the integrated scramjet-powered vehicle.

References

[1] Barthelemy, R. R., "The National Aero-Space Plane Program," AIAA Paper 89-5001, July 1989.

[2] Schweikart, L., *The Hypersonic Revolution-Case Studies in the History of Hypersonic Technology*, Vol. 3, U.S. Air Force Bolling AFB, Washington, D.C., 1998.

[3] White, A. W., Engelund, W. C., Stanley, D. O., Naftel, J. C., Lepsch, R. A., Bush, L. B., and Wurster, K. E., "Technology and Staging Effects on Two-Stage-to-Orbit Systems," *Journal of Spacecraft and Rockets*, Vol. 31, No. 1, 1994, p. 31. doi:10.2514/3.26399

[4] Mehta, U. B., and Bowles, J. V., "A Two-Stage-to-Orbit Spaceplane Concept with Growth Potential," *Journal of Propulsion and Power*, Vol. 17, No. 6, 2001, pp. 1149–1161.

[5] Isakowitz, S. J., *International Reference Guide to Space Launch Systems*, AIAA, Reston, VA, 1995.

[6] O'Shaunessy, J. D., Pinckney, S. Z., McMinn, J. D., Cruz, C. I., and Kelley, M., "Hypersonic Vehicle Simulation Model: Winged-Cone Configuration," NASA TM 102610, 1990.

[7] Phillips, W. P., Brauckmann, G. J., Micol, J. R., and Woods, W. C., "Experimental Investigation of the Aerodynamic Characteristics for a Winged-Cone Concept," AIAA paper 87-2484, 1987.
[8] Lewis, M. J., "Significance of Fuel Selection for Hypersonic Vehicle Range," *Journal of Propulsion and Power*, Vol. 17, No. 6, 2001, pp. 1214-1221.
[9] Prusha, L., "Trajectory Optimisation for a Small Launch Vehicle with a Scramjet Powered Second Stage," M.Eng.Sc. Thesis, Dept. of Mechanical Engineering, Univ. of Queensland, Queensland, Australia, 1997.
[10] Smart, M. K., "Design of Three-Dimensional Hypersonic Inlets with Rectangular-to-Elliptical Shape Transition," *Journal of Propulsion and Power*, Vol. 15, No. 3, 1999, pp. 408–416. doi:10.2514/2.5459
[11] Smart, M. K., and Ruf, E. G., "Free-Jet Testing of a REST Scramjet at Off-Design Conditions," AIAA Paper 2006-2955, June 2006.
[12] Burkhardt, J., "REENT6D a Simulation and Optimization Tool for Re-Entry Missions," Inst. for Space Systems Rept. IRS-01B7, Stuttgart, Germany, 2000.
[13] Regan, F. J., and Anandakrishnan, S. M., *Dynamics of Atmospheric Re-Entry*, AIAA Education Series, AIAA, Reston, VA, 1993.
[14] Tetlow, M., "Commercial Launch Vehicle Design and Predictive Guidance Development," Ph.D. Dissertation, School of Mechanical Engineering, Univ. of Adelaide, Adelaide, Australia, 2003.
[15] Suraweera, M. V., and Smart, M. K., "Shock Tunnel Experiments with A Mach 12 REST Scramjet at Off-Design Conditions," AIAA Paper 2008-0100, 2008.
[16] Heiser, W. H., and Pratt, D. T., *Hypersonic Airbreathing Propulsion*, AIAA Education Series, AIAA, Reston, VA, 1994.
[17] White, J. A., and Morrison, J. H., "A Pseudo-Temporal Multi-Grid Relaxation Scheme for Solving the Parabolized Navier-Stokes Equations," AIAA Paper 99-3360, Jan. 1999.
[18] Smart, M. K., "Experimental Testing of a Hypersonic Inlet with Rectangular-to-Elliptical Shape Transition," *Journal of Propulsion and Power*, Vol. 17, No. 2, 2001, pp. 276–283. doi:10.2514/2.5774
[19] Smart, M. K., "Scramjets," *The Aeronautical Journal*, Vol. 111, No. 1124, 2007, pp. 605–619.
[20] Ortwerth, P. J., "Scramjet Vehicle Integration," *Scramjet Propulsion*, Progress in Astronautics and Aeronautics, AIAA, Washington, D.C., 2001, Chap. 17.

J. Martin
Associate Editor